Effectively boosting selective ammonia synthesis on electron-deficient surface of MoB_2

Hong Yu Zhou [1], Yan Bin Qu [1], Jian Chen Li, Zhi Li Wang, Chun Cheng Yang [*], Qing Jiang [*]

Key Laboratory of Automobile Materials, Ministry of Education, and School of Materials Science and Engineering, Jilin University, Changchun 130022, China

A R T I C L E   I N F O

A B S T R A C T

Carbon-free electrocatalytic nitrogen reduction reaction (NRR) is an attractive replacement of the current Haber-Bosch method. However, there is a lack of suitable electrocatalysts that simultaneously achieve both high activity and selectivity, hindering the practical applications of NRR. Herein we theoretically design an electron-deficient surface of MoB_2 for preferential N_2 adsorption and thus increase the local concentration of N_2 around the active sites. These lead to outstanding NRR selectivity that can evidently retard the competing HER even at the NRR operating potential. The corresponding theoretical limiting potential for NRR is as low as -0.34 V. Our proof-of-concept experiment confirms the above theoretical design, in which excellent NRR performances (NH_3 yield rate of ~ 40.94 µg h^{-1} mg^{-1}, FE of $\sim 30.84\%$) have been achieved. The strategy of inducing electron deficiency on active sites provides new insight into the rational design of NRR electrocatalysts for realizing green and effective ammonia synthesis in practical applications.

1. Introduction

In addition to as a key raw material for producing fertilizers, plastic, pharmaceuticals and so on, ammonia (NH_3) also serves as an ideal carbon-free energy carrier with a high energy density due to the easily liquefied property under mild conditions and high hydrogen content (17.6 wt%) [1,2]. Moreover, the corresponding infrastructures for storing and transporting liquid ammonia are well-established [3]. Industrially, NH_3 synthesis dominated by the traditional Haber-Bosch (H-B) process shows drawbacks like heavy energy consumption, poor energy conversion efficiency and harmfully CO_2 emission [4,5]. Thus, there exists a palpable requirement for developing an economical and environmentally friendly route to replace the H-B process. Using water as the hydrogen source, electrochemical nitrogen reduction reaction (NRR) offers a renewable energy driven pathway to produce NH_3 at ambient conditions because of its low energy consumption, potentially high energy efficiency and environment friendliness [6].

Unfortunately, two significant challenges associated with electrochemical NRR still remain unsolved. On one hand, N_2 as a non-polar diatomic molecule with a strong triple bond (941 kJ/mol) is inert towards hydrogenation, leading to a sluggish reaction kinetics and thereby very low NH_3 yields [3,7]. On the other hand, owing to the low solubility of N_2 in electrolyte, there are overwhelming protons and low local concentration of N_2 around the catalyst surface, giving rise to a tough reaction selectivity issue (low Faradaic efficiency, FE). Transition metals (TM) are generally regarded as promising catalysts for N≡N bond activation, which can be attributed to the partially occupied d orbitals inducing strong π backdonation [8]. However, because of the preferential adsorption of H$^+$ over N_2 on the surface, electrochemical NRR on virtually all TM catalysts is inhibited by the intense competition from hydrogen evolution reaction (HER), which hammers the FE of NRR severely [9]. Thus, the simultaneous satisfaction of activity and selectivity could not be realized technically so far.

To promote NRR process efficiently and selectively, the modulation of the electronic structure of active TM atoms on a catalyst surface to strengthen the intrinsic N_2 adsorption capacity should be an effective strategy to overcome the above challenges. An active TM site with local electron deficiency (TM$^{\delta+}$) that can facilitate the electron transfer from the lone-pair electrons of N_2 to empty d orbitals should be able to improve the NH_3 synthesis selectivity by boosting N_2 adsorption. The enhancement of adsorption capacity can accelerate the N_2 mass transfer to achieve a high local centration of N_2 around the catalyst in aqueous solution and then improve the possibility of molecular collisions, reducing the reaction energy during NRR process [10].

Boron, an electron-deficient atom with three valence electrons distributing in four orbitals, is a suitable element for inducing electron-deficient sites. Experiments reported that B atom doping in graphene framework induces electron redistribution, where the electron-deficient B sites exhibit enhanced N_2 adsorption and poor binding strength with proton for HER [11,12]. Xiao et. al. found that the TM atom coordinated with four B atoms (MB_4) could give a better NRR performance than that did with four C or N atoms [13].

Transition metal diborides (TMB_2), by virtue of their high electrical conductivity and good stability in both acidic and basic solutions, have garnered extensive attention as promising electrocatalysts [14–16]. Nevertheless, despite the fact that Mo species has high NRR activity in light of numerous experimental and computational works, studies on MoB_2 as an NRR electrocatalyst are little. MoB_2 has a MXene-like layered structure formed by planar metal and boron layers, indicating that there are abundant Mo sites on the surface when the Mo layer is exposed [14]. The unique electron structure of B atom promotes the transfer of valence electrons of Mo, introducing electron-deficient Mo-terminated surface with abundant active site.

Herein, we report a theoretical study to improve both the selectivity and activity of NRR by using the electronic deficient surfaces of MoB_2. Our results show that the positively charged Mo-terminated surface [Mo-(001)] is the most energetically favorable surface of MoB_2, indicating multitudinous active sites on the surfaces. Strikingly, the positively charged Mo sites have a stronger adsorption capability for N_2 than H^+ even applying the NRR operating potential, suggesting that the competitive HER is effectively suppressed. Therefore, the NRR becomes a favorable reaction pathway with a low reaction free energy of -0.34 eV on Mo-(001) surface. In addition, proof-of-concept experiment reveals that MoB_2 exhibits superior intrinsic catalytic activity for NRR with an NH_3 yield of 40.94 ± 0.97 $\mu g\,h^{-1}\,mg^{-1}$ (-0.4 V vs. RHE) and an FE of $30.84 \pm 0.91\%$ (-0.3 V vs. RHE), both show the best overall catalytic performance among the known NRR catalysts, simultaneously achieves high activity and selectivity.

2. Experimental section

2.1. Calculational detail

In this work, all calculations are performed by employing the spin-polarized Density Functional Theory (DFT) method with the Cambridge Serial Total Energy Package (CASTEP) code based on the ultrasoft pseudopotentials [17,18]. The exchange-correlation effects are described by the generalized gradient approximation (GGA) with Perdew-Burke-Ernzerhof exchange-correlation functional [19]. The van der Waals interactions are considered by the DFT-D2 method within the Grimme scheme [20]. The cutoff energy for plane-wave expansion is set to 400 eV and the convergence criteria of the geometrical optimization are set to be 1.0×10^{-5} eV/atom, 0.03 eV/Å, and 0.001 Å for the energy change, maximum force, and maximum displacement, respectively. The corresponding k-point sampling of the Brillouin zone is set as $3 \times 3 \times 1$ grid. To investigate the nature of bonding between Mo and intermediates, the crystal orbital Hamilton population analysis was performed [21–23].

The (100) and (001) surfaces of MoB_2 with different terminations are taken for evaluating the stability and the catalytic activity for NRR. These surfaces can be obtained by cleaving the bulk MoB_2 structure with the corresponding planes. The surface model contains the surface dimension of 3×3 repeated unit cell and the thickness of six atomic layers, in which the upper two layers are fully relaxed while the bottom layers being fixed during the calculations, and a vacuum distance of 15 Å is chosen to avoid the interactions between two periodic images. The surface energy (γ) is evaluated by [24],

$$\gamma = \frac{E_{\text{slab}}^{\text{relaxed}} - nE_{\text{bulk}}}{A} - \frac{E_{\text{slab}}^{\text{unrelaxed}} - nE_{\text{bulk}}}{2A} \tag{1}$$

where the $E_{\text{slab}}^{\text{relaxed}}$, $E_{\text{slab}}^{\text{unrelaxed}}$ and E_{bulk} denote the total energy of the slab (only relaxed on one side), that of the unrelaxed slab, and that of the bulk MoB_2 formula unit, and n is the number of MoB_2 units in the slab. The parameter A shows the surface area of one side of the slab model. The first term in Eq. (1) is a sum of γ of top surface and forming energy of the unrelaxed bottom surface. The latter is the forming energy of the unrelaxed bottom surface which equals to half of $\frac{E_{\text{slab}}^{\text{relaxed}} - nE_{\text{bulk}}}{A}$, namely the second term in Eq. (1). The difference of two terms consists of Eq. (1). The adsorption energies ($\Delta E_{*\text{x}}$) of intermediate species were defined by,

$$\Delta E_{*\text{x}} = (E_{\text{t}} - E_{\text{x}} - E_*) \tag{2}$$

where E_{t}, E_{x}, and E_* are total energies of the catalyst with adsorbed species, the adsorbed species, and the catalyst surface, respectively. The average N_2 adsorption energy ($\Delta E_{*\text{x}}$) was determined by,

$$\Delta E_{\text{avg-N2}} = \frac{\Delta E_{*\text{N2}}}{n} \tag{3}$$

where the n is the number of Mo atoms contained in the active site. Moreover, The calculations of Gibbs free energy change (ΔG) of every elemental step was based on a computational hydrogen electrode (CHE) model proposed by Nørskov et al. during the NRR process [25–27]. The reference potential set to be RHE, which uses one half of chemical potential of H_2 as the chemical potential of the proton-electron pair. The value of ΔG can be calculated by,

$$\Delta G = \Delta E + \Delta E_{\text{ZPE}} - T\Delta S \tag{4}$$

where ΔE, ΔE_{ZPE}, ΔS, T are the values of the reaction energy, the zero-point energy (ZPE), the entropy difference between products and reactants and the temperature (298.15 K in this work), respectively. For the gas-phase molecule (N_2 and NH_3), the entropy term was taken from the standard values of thermodynamics [28]. In addition, the limiting potential (U_{L}) can be calculated by.

$$U_{\text{L}} = -\Delta G_{\text{max}}/e \tag{5}$$

where ΔG_{max} represents the most positive free energy change of each elementary step during the NRR process. Besides, the difference of adsorption free energy for N_2 and H^+ at 0 V vs. RHE (δG) and at the U_{L} of NRR (δG^{lim}) can be calculated by

$$\delta G = \Delta G_{*\text{N2}} - \Delta G_{*\text{H}} \tag{6}$$

$$\delta G^{\text{lim}} = \Delta G_{*\text{N2}} - [\Delta G_{*\text{H}} + eU_{\text{L}}] \tag{7}$$

where $\Delta G_{*\text{N2}}$ and $\Delta G_{*\text{H}}$ represent the adsorption free energy of N_2 and H^+ on the active sites at 0 V vs. RHE, respectively.

2.2. Synthesis of MoB_2

Molybdenum diboride (MoB_2, 99.5%) and sodium hypochlorite solution (NaClO, available Cl 4.0%) were purchased from Shanghai Macklin Biochemical Co., Ltd. Sodium hydroxide (NaOH, 96.0%), trisodium citrate dihydrate ($C_6H_5Na_3O_7 \cdot 2H_2O$, 99.0%), salicylic acid ($C_7H_6O_3$, 99.5%), sodium sulfate (Na_2SO_4, 99.0%), ammonium chloride (NH_4Cl, 99.5%) were got from Sinopharm Chemical Reagent Co., China. Isopropyl alcohol (C_3H_8O, 99.5%) and P-dimethylaminobenzaldehyde (PDAB, $C_9H_{11}NO$, 99%) were purchased from Shanghai Aladdin Biochemical Technology Co., Ltd. Hydrochloric acid (HCl, 35.0–38.0%), hydrogen peroxide (H_2O_2, 30%), and ethanol (C_2H_5OH, 99.7%) were obtained from Beijing Chemical Works, China. Perfluorinated resin solution containing Nafion (5 wt%) was obtained from Sigma-Aldrich Co. Hydrazine monohydrate ($N_2H_4 \cdot H_2O$, 80.0%) was got from Adamas-beta Chemical Co. Nitrogen (N_2, high purity 99.999%) and argon (Ar, high purity 99.999%) were purchased from Ju'yang gas Co., China. The ultrapure water with a resistivity of 18.2 MΩ cm was used in all experiments. All of the chemicals were used without further purification.

2.3. Characterizations

Microstructure characterizations and chemical component analysis of nanosheet catalyst electrodes were performed on a field-emission scanning electron microscope (JSM-6700F, JEOL, 7 keV), and a field-emission transition electron microscope (JEM-2100F, JEOL) equipped with X-ray energy-dispersive spectroscopy (EDS). XRD measurements of nanosheet catalyst were conducted on a D/max2500pc diffractometer with a monochromated Cu Kα radiation. Chemical states and distribution of surface elements were analyzed using XPS on a Thermo ECSALAB 250.

2.4. Preparation of electrode

A homogeneous ink was prepared by mixing 5 mg of MoB_2 powders into 1 mL water/isopropanol solution (V:V = 1:3, containing 40 μL 5 wt % Nafion solution), followed by sonication for 30 min. The electrode was manufactured by loading the above ink onto a carbon paper (1 cm × 2 cm) and drying under ambient conditions with a loading of 0.1 mg cm^{-2}.

2.5. Electrochemical measurements

The NRR tests were performed in a two-compartment cell separated by a Nafion membrane under ambient condition. The membrane was boiled in H_2O_2 (5 wt%) aqueous solution, 0.5 M H_2SO_4 and ultrapure water at 80 °C for 1 h, respectively [29]. Electrochemical tests were carried out with an Ivium-n-Stat electrochemical analyzer (Ivium Technologies, Netherlands) using a three-electrode with prepared electrodes, platinum plate and Ag/AgCl (filled with saturated KCl solution) electrode as working electrode, counter electrode and reference electrode, respectively. All potentials were measured against an Ag/AgCl reference electrode and converted to the RHE reference scale using the equation: E (vs. RHE) = E (vs. Ag/AgCl) + 0.197 V + 0.0591 × pH. Prior to the NRR tests, all electrolytes were purged with Ar and N_2 for 30 min, respectively. During the NRR electrolysis, pure N_2 was continuously fed into the cell.

The salicylic acid analysis method was used to quantify the concentration of NH_3 in 0.1 M Na_2SO_4 solution via UV–vis spectrophotometry [30]. Firstly, calibration curve was obtained by ammonia chloride concentration-dependent UV–vis absorption spectrum. 1.0 μg mL^{-1} NH_4^+ solution in 0.1 M Na_2SO_4 was prepared used NH_4Cl as raw material, and then diluted with 0.1 M Na_2SO_4 to get a series of reference solutions from 0 to 1.0 μg mL^{-1}. Typically, 50 μL of oxidizing solution, which composed of NaClO (0.05 M) and NaOH (0.75 M) aqueous solution, 500 μL of coloring solution containing 0.4 M salicylic acid and 0.32 M NaOH and 50 μL of catalyst solution that prepared by diluting 0.1 g of sodium nitroferricyanide dihydrate to 10 mL with deionized water, were added in to the 4 mL of the electrolyte solution in turn. After two hours away from light, the absorbance at λ = 658 nm was collected and plotted. The concentration of NH_3 after electrolysis two hours was acquired via the calibration curve.

The concentration of hydrazine hydrate (N_2H_4) was determined by the Watt and Chrisp method [31]. The color developing agent was the miscible liquids of Para-(dimethylamino) benzaldehyde (5.99 g), HCl (12 M, 30 mL) and ethanol (300 mL). 2 mL electrolyte mixed with 2 mL of the chromogenic reagent was added and under the dark for 30 min. The background correction was carried out using 0.1 M Na_2SO_4 solution. The absorbance at λ = 457 nm was measured and plotted. A linear fit was generated from the standard measurements and used to calculate the concentrations of N_2H_4.

2.6. Calculation of NH_3 yield and Faradaic efficiency

The NH_3 yield rate could be calculated as:

$$\text{yield rate} = \frac{C \times V}{t \times m} \tag{8}$$

The Faradaic efficiencies of products solution were determined using followed equation:

$$FE = \frac{3 \times F \times C \times V}{17 \times Q} \tag{9}$$

where the C, V, t, m F and Q are the measured concentration of NH_3 (μg mL^{-1}) after electrolyze 2 h, the volume on the Na_2SO_4 electrolyte (mL), the run time (2 h), the loading mass of catalyst (mg), the faradaic constant (96,485) and the quantity of electronic transferred during electrocatalytic reaction period, respectively.
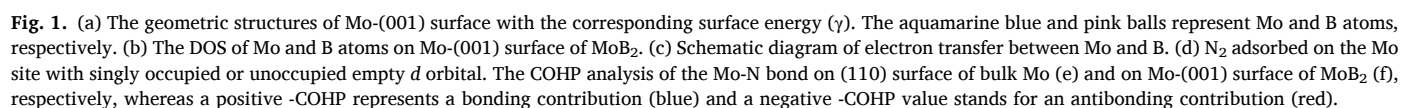
3. Results and discussion

3.1. Geometry structure of MoB_2

The first (*N_2 → *NNH) or the last (*NH_2 → *NH_3) hydrogenation steps could usually be the potential limiting step (PLS) of NRR. Thus, the corresponding reaction free energies [$\Delta G_{(*N2-*NNH)}$ and $\Delta G_{(*NH2-*NH3)}$] were calculated to evaluate the NRR performance of various transition metal diborides (TMB$_2$, TM = Ti, V, Cr, Zr, Nb and Mo). The results show that the MoB_2 exhibits a negative $\Delta G_{(*N2-*NNH)}$ of − 0.08 eV and the lowest $\Delta G_{(*NH2-*NH3)}$ of 0.21 eV among all these candidates (Fig. S1), suggesting that MoB_2 could effectively stabilize *NNH and destabilize *NH_2. Hereby, the MoB_2 was chosen as a promising candidate for further discussion.

The crystal structure of bulk MoB_2 can be viewed as a sandwich-like configuration comprising borophene inserted Mo based 3D frameworks. The main exposed crystal facets are (100) and (001) with Mo- and B-terminations [Mo-(100), B-(100), Mo-(001) and B-(001)] based on the previous studies and our experiment evidences [14,32]. The corresponding surface energy values (γ) calculated bu Eq. (1) are γ$_{Mo-(100)}$ = 3.27 J/m^2, γ$_{B-(100)}$ = 3.36 J/m^2, γ$_{Mo-(001)}$ = 2.99 J/m^2, γ$_{B-(001)}$ = 3.51 J/m^2, respectively. Since the γ value of Mo-(001) surface is the smallest, it will be chosen for evaluating NRR performances of MoB_2 in the following. As is illustrated in Fig. 1a, the Mo atoms of Mo-(001) surface are directly above the centers of boron six-membered rings where Mo—B and Mo—Mo bond lengths are 2.23 and 3.01 Å, respectively. The density of states (DOS) of surface Mo and B atoms are shown in Fig. S2. The hybridization between the orbitals of Mo and B is evident, indicating strong chemical bonds between Mo and B atoms, being conducive to the electron transfer in the system.

3.2. Role of Mo and B

To explore the surface electronic property of Mo-(001) surface, the partial DOS (PDOS) of Mo atom was calculated (Fig. 1b). The PDOS of Mo reveals that the $4d_{z}^{2}$ orbital is above the Fermi level, implying its unoccupied state. This is mainly because the $4d$-orbital electrons transfer from Mo to B atoms and thus induce the above phenomenon in the surface Mo atom, as depicted in Fig. 1c. The distinct electron depletion regions around Mo atoms can be clearly observed in the atomic electron density maps (Fig. S3). It is noteworthy that the d electrons of Mo are not excessively depleted due to the similar electronegativity values of Mo (2.16) and B (2.04). The Hirshfeld population analysis implies that the surface Mo atoms have positive charge of + 0.23 e. For comparison, the Mo atom charge values of pure metal Mo, the Mo-edge of MoS_2 and MoO_2 calculated are 0, + 0.23 and + 0.66 e, respectively. Thus, the electropositive degree obeys an order of pure metal Mo < MoS_2 = Mo-(001) < MoO_2, denoting that the valence of the surface Mo atoms of MoB_2 is situated between low valence state of 0 and + 4. These moderate electron-deficiency Mo site (Mo$^{\delta+}$) without excessive electron loss do not hinder the injection of electrons from the

Fig. 1. (a) The geometric structures of Mo-(001) surface with the corresponding surface energy (γ). The aquamarine blue and pink balls represent Mo and B atoms, respectively. (b) The DOS of Mo and B atoms on Mo-(001) surface of MoB_2. (c) Schematic diagram of electron transfer between Mo and B. (d) N_2 adsorbed on the Mo site with singly occupied or unoccupied empty d orbital. The COHP analysis of the Mo-N bond on (110) surface of bulk Mo (e) and on Mo-(001) surface of MoB_2 (f), respectively, whereas a positive -COHP represents a bonding contribution (blue) and a negative -COHP value stands for an antibonding contribution (red).

Mo-4d orbitals into the N$_2$-π^* orbitals for activation, implying the potential for high NRR catalytic activity.

During the N$_2$ adsorption process, the d electron backdonation process has been focused on while the step of accepting lone-pair electrons from N$_2$ molecule was ignored [33]. Actually, the latter is more important because it determines whether N$_2$ molecule can be preferentially adsorbed on the surface and achieve a high local concentration of N$_2$ around the active sites, promoting a great N$_2$ coverage [10,34]. Since the Mo$^{\delta+}$ sites possess empty d orbitals, it would bypass unfavorable σ antibonding and additional exchange repulsion from the occupied orbital as the N$_2$ approaching, namely, favorite Mo-N bond formation (Fig. 1d and Note S1). The surface Mo atoms of Mo-(001) and that of pure metal Mo (110) were used to represent Mo^0 and Mo$^{\delta+}$ sites, respectively. Noted that the optimal N$_2$ adsorption configuration of pure Mo (110) surface is the hollow site consisting of 4 Mo atoms (H$_4$ site, Fig. S4) while that of Mo-(001) surface of MoB$_2$ is the hollow site containing 3 Mo atoms (H$_3$ site, see the discussion below for details). Considering there exists H$_4$ sites on Mo-(001) surface, the initial model for the N$_2$ adsorbed at the H$_4$ site on Mo-(001) surface was established. As shown in Fig. S5, during the geometry optimization process, the N$_2$ spontaneously moves from the H$_4$ to H$_3$ site, suggesting that the H$_3$ site is the stable adsorption site for Mo-(001) surface, while H$_4$ site is unstable. Thus, the average adsorption energy values of N$_2$ ($\Delta E_{\text{avg-N2}}$) on Mo^0 and Mo$^{\delta+}$ sites are -0.67 and -0.79 eV, respectively, suggesting that the Mo$^{\delta+}$ site has a better N$_2$ affinity.

Furthermore, the crystal orbital Hamilton population (COHP) was performed to quantitatively investigate the bonding-antibonding property of the Mo^0/Mo$^{\delta+}$—N bond. As depicted in Figs. 1e and 1f, the Mo^0—N bond has more filled antibonding orbitals than Mo$^{\delta+}$—N bond does, which is consistent with our above analysis.

3.3. N$_2$ adsorption and activation

There are two possible adsorption configurations for N$_2$ (end-on and side-on configurations), in which the end-on configuration denotes the adsorption on the top site, and the side-on configuration does on bridge or hollow sites. As shown in Fig. 2a, the adsorption energy values ($\Delta E_{\text{*N2}}$) of N$_2$ are -1.68 eV, -1.98 eV, and -2.36 eV for top, bridge, and hollow sites, and the corresponding N≡N bond lengths are elongated from 1.16 Å (free N$_2$ molecule) to 1.18 Å, 1.25 Å and 1.31 Å, respectively. Hence, the N$_2$ molecule is significantly activated on the electron-deficient Mo-(001) surface. In light of the Hirshfeld charge analysis result, there is significant charge transfer (0.32 e) from Mo to N$_2$ molecule when N$_2$ is adsorbed at the hollow site [if N$_2$ is adsorbed on the top and bridge sites, the corresponding data are 0.13 and 0.25 e], confirming that the best activating site is the hollow one, which is in line with the adsorption energy trend (the more electrons are transferred, the stronger is the adsorption) [35].

To further verify the activation degree of N$_2$ molecule, the COHP of N≡N bond was calculated (Fig. 2b). The electrons from the catalyst fill the antibonding orbital of the N≡N bond when N$_2$ is adsorbed at active sites. Furthermore, we integrated the crystal orbital Hamilton population (ICOHP) up to Fermi level to quantitatively depict the N$_2$ activation [the less negative the ICOHP is, the more activated is the N$_2$]. The order of ICOHP values was hollow-N$_2$ (-7.30) > bridge-N$_2$ (-8.95) > top-N$_2$ (-10.64) > free N$_2$ (-11.39), denoting that the hollow site could most effectively weaken the N≡N bond with a considerable antibonding orbital filling among three sites. Therefore, N$_2$ molecule prefers to be adsorbed at hollow site of Mo-(001) and then be effectively activated to be radical-like, which is active for protons.

To elucidate the bonding nature of N$_2$ activation, we analyzed the interaction between the hollow site and N$_2$ by plotting the partial density of states (PDOS) before and after the adsorption (Fig. 2c). The results reveal that N-2s and -2p orbitals are overlapped with the Mo-4d orbitals, indicating their easy hybridization. Clearly, the Mo-4d orbitals accept the lone pair electrons of N$_2$ molecule, forming the bonding states that

strengthen the N$_2$ adsorption. Simultaneously, the occupied 4d orbitals of Mo interact with the N$_2$ empty 2π^* orbital, resulting in that their hybridized energy levels split into two groups near the Fermi level. One is the bonding states that are occupied under the Fermi level, d-$\pi^*_{\text{(occ)}}$, and another is the unoccupied one that lies above the Fermi level, d-$\pi^*_{\text{(unocc)}}$. The obvious electron transfer process between Mo and N atoms can also be observed by the plot of the charge density difference (Fig. 2d).

3.4. Electrochemical performance

Theoretically, the intrinsic activity of the electrocatalysts can be estimated by U_L, the minimum applied potential to ensure that all protonation reactions are exergonic. Since the side-on adsorption configuration on Mo-(001) surface is more favorable thermodynamically, the end-on pattern for N$_2$ adsorption is not considered in the following. There are three possible associative NRR catalytic mechanisms for the side-on pattern appearing possibly on the surfaces [36], including consecutive (protonation consecutively occurs on one end of N$_2$), enzymatic (protonation alternately occurs at both N atom of N$_2$), and mixed mechanisms (protonation steps along with enzymatic mechanism until form *NHNH$_2$, and then shuttle to the consecutive mechanism), which are plotted in Fig. 3a.

For the Mo-(001) surface of MoB$_2$, the N$_2$ molecule is likely adsorbed at the hollow site with $\Delta G_{\text{*N2}} = -1.83$ eV, and the protonation steps prefer to the mixed mechanism (Fig. 3b). The first three hydrogenation processes of NRR are identical with the enzymatic mechanisms. The ΔG values for the formations of *NNH, *NHNH and *NHNH$_2$ species are -0.08, -0.41 and 0.12 eV, respectively. Then, the (H$^+$ + e$^-$) consecutively attack the *NH$_2$ part of *NHNH$_2$ to generate *NH, and release the first NH$_3$ with $\Delta G = -0.89$ eV. Moreover, the ΔG values for *NH$_2$ and *NH$_3$ formations are 0.34 and 0.21 eV, respectively. Therefore, the formation of *NH$_2$ (*NH + H$^+$ + e$^-$ → *NH$_2$) is the potential limiting step with the maximal ΔG value of 0.34 eV and $U_L = -0.34$ V vs. RHE. Also, the ΔG diagrams and corresponding intermediate configurations of the consecutive and enzymatic mechanisms are shown in Fig. S6. The corresponding U_L values are -0.34 and -1.36 V for consecutive and enzymatic mechanisms, respectively.

Generally, catalysts with high NRR activity always have a strong adsorption capability for N species, which makes desorption of NH$_3$ difficult. Although the Mo-(001) surfaces possess a strong N$_2$ adsorption ability, interestingly, the adsorbed site changes from hollow site to the bridge site, and finally to the top site during the protonation steps from *NH to *NH$_3$, indicating gradual weakening of adsorption capacity for N species, which contributes to desorption of *NH$_3$ (Fig. 3b). The desorption free energy $\Delta G_{\text{(NH3)}}$ value of Mo-(001) surface is 1.19 eV that is lower than that of experimentally prepared NRR electrocatalysts with high performance, such as B-MoS$_2$ (1.31 eV) [37], B@Mo$_2$CO$_2$ (2.0 eV) [38], W-N$_4$ (1.32 eV) [39] and so on, suggesting the recycle of NRR can be carried out experimentally, as demonstrated by our experimental results below. This is mainly because the *NH$_3$ species could be readily protonated to form NH$_4^+$ under the acid or alkalescency conditions, which is easily soluble in aqueous electrolyte and regenerate the catalytic active sites.

3.5. Reaction selectivity toward NH$_3$ synthesis

Apart from the high catalytic activity, an ideal NRR electrocatalyst should also prevent the unfavorable O-containing species (O, OH and H$_2$O) poisoning and inhibit the competitive reaction of HER for the high FE during the NH$_3$ synthesis process. Herein, the ΔG of possible O-containing species adsorbed on Mo-(001) surface were calculated and the corresponding geometric configurations are given in Fig. S7. The corresponding adsorption free energies of O, OH and H$_2$O species are -1.58, -1.25 and -0.94 eV, respectively, which are more positive than the $\Delta G_{\text{*N2}}$ (-1.83 eV), implying preference of N$_2$ adsorption in

(a)

(b)

(c)

(d)
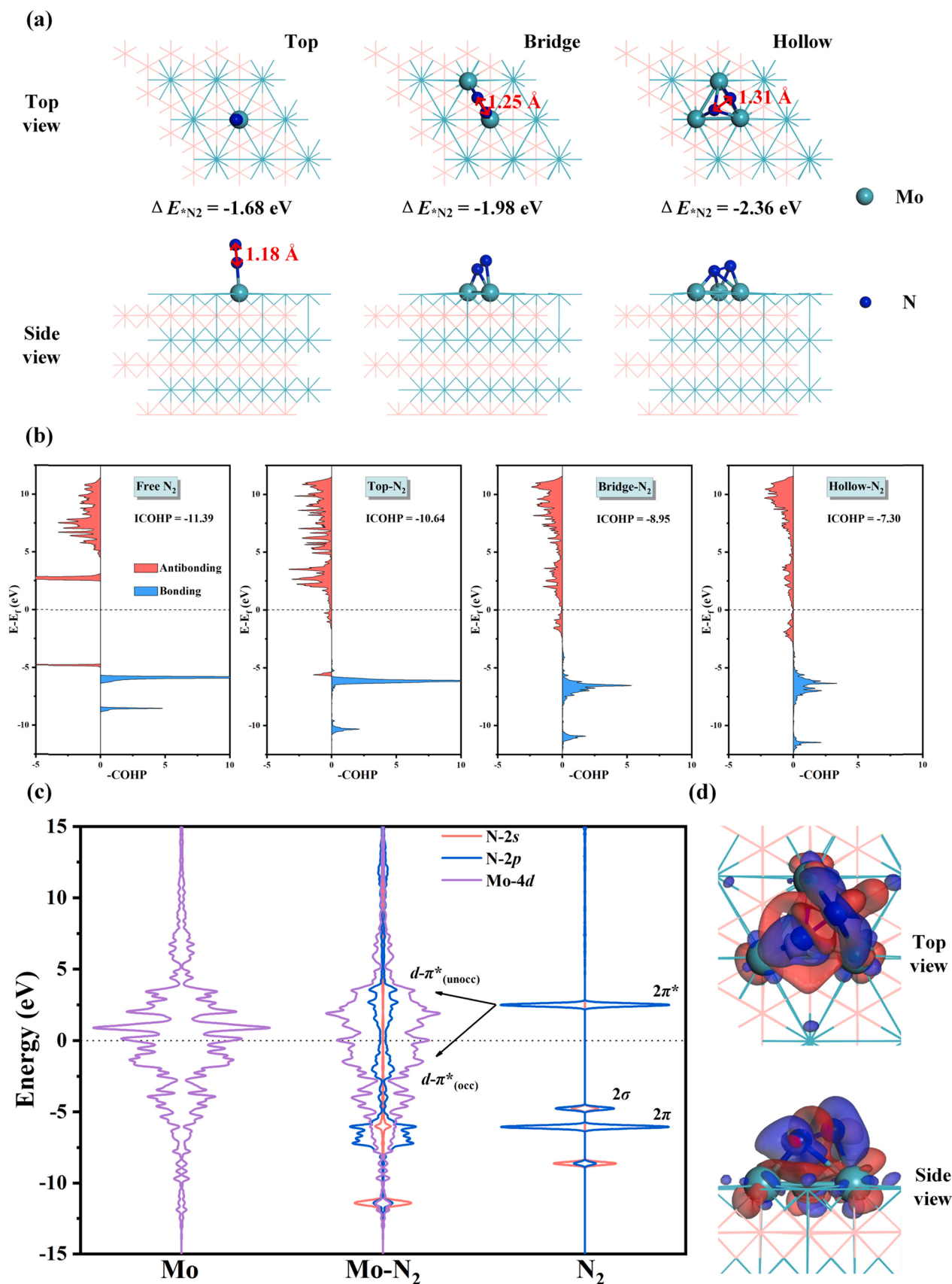
Fig. 2. (a) The top and side views for N_2 adsorbed at different adsorption sites on Mo-(001) surface and the corresponding adsorption energy values. (b) The COHP for N—N bond of free N_2 molecule, adsorbed N_2 at top, bridge and hollow sites. (c) The PDOS of Mo atoms on Mo-(001) surface, N_2 adsorbed at hollow site and N_2 gas molecule. (d) The electron density difference of N_2 adsorbed at hollow site of Mo-(001) surface, where blue and red indicate electron density accumulation and depletion, respectively.
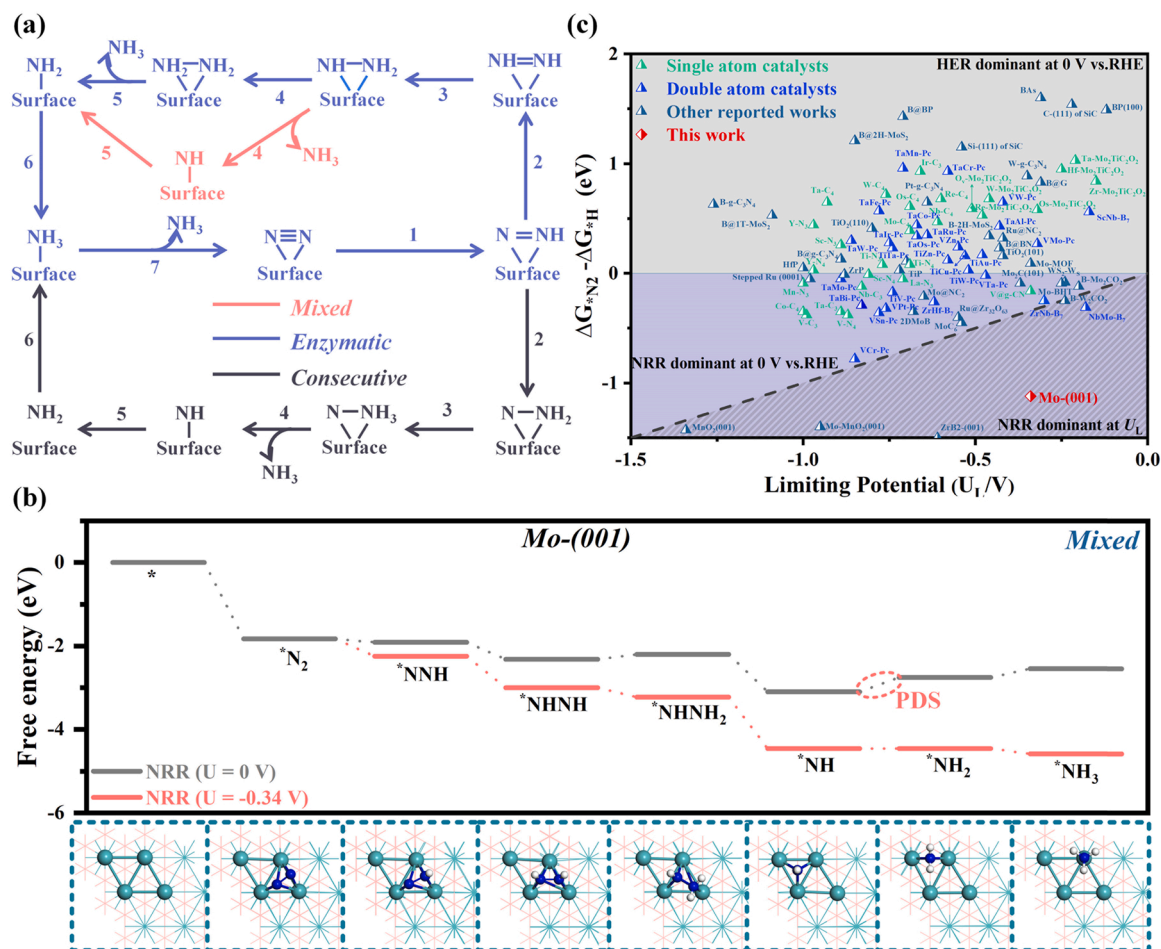
Fig. 3. (a) Schematic illustration of the possible reaction mechanisms during the N$_2$ reduction through side-on adsorption pattern. (b) The Gibbs free energy change diagram for NRR and the corresponding adsorption configuration of intermediates on Mo-(001) surface. (c) The plot of U_L vs. δG ($\Delta G_{*N2} - \Delta G_{*H}$) on Mo-(001) surface and other reported catalysts. The grey and purple regions correspond to the *H and *N$_2$ dominant region at 0 V vs. RHE, respectively. For those electro-catalysts in purple area, they can exhibit good selectivity for NRR at 0 V vs. RHE. while will be blocked by the H$^+$ at the U_L of the NRR. For the electrocatalysts in the shade area, the competing HER can be largely inhibited on their active sites even at the NRR operating potential.

aqueous solution. Besides, the *O on the surface could be reduced by the protons and could form *OH (*O + H$^+$ + e^- → *OH), which then transforms to *H$_2$O species (*OH + H$^+$ + e^- → *H$_2$O) with low ΔG values of 0.33 and 0.31 eV, respectively (Fig. S8). As results, the possible O-containing species could be easily removed from the surface and the surface is dominantly covered by N$_2$ during the activation process of electrochemical measurement, as demonstrated in literatures [35,40].

For the most metallic facets, the H$^+$ could easily block the active sites and go towards the HER rather than the NRR, leading to a low FE [41, 42]. Here, the H$^+$ adsorption free energy (ΔG_{*H}) on the Mo sites of Mo-(001) surface was calculated of − 0.71 eV (Fig. S9), which is more positive than the ΔG_{*N2} value. Thus, N$_2$ rather than H$^+$ is likely to adsorbed on the active sites without applied potential. Evidently, the electron-deficient Mo site contributes to this excellent selectivity. Additionally, under the electrochemical NRR conditions, the H$^+$ adsorption will be promoted by a negative electrode potential due to the involvement of proton and electron transfer, while N$_2$ have been little affected [41,43–45]. Herein, we used the δG^{lim} to describe the adsorption selectivity at the corresponding U_L of NRR. The negative value of δG^{lim} (− 0.78 eV) implies that the active site still preferentially adsorbs N$_2$ instead of H$^+$ at NRR operating potentials, suggesting a great selectivity towards NRR at the electrochemical ambient.

To comprehensively evaluate the catalytic performance of Mo-(001) facet, the relationships of δG vs. U_L are shown in Fig. 3c, and the relevant data from references are given too for a comparison purpose (Table S1).

The grey or purple region corresponds to the *H or *N$_2$ dominant region at 0 V vs. RHE, respectively. The shaded area suggests that the active sites of electrocatalysts have a great selectivity toward NH$_3$ at their corresponding U_L of the NRR. Consequently, the position of Mo-(001) surface suggests a remarkable selectivity toward NH$_3$ and a smaller U_L value than other electrocatalysts in the shade area, which not only exhibits much higher selectivity than the recently reported NRR catalysts, but also maintains outstanding catalytic activity.

3.6. Proof-of-concept experiment

The above theoretical predictions are experimentally confirmed where the commercial MoB$_2$ particles are taken as electrocatalysts for NRR. Scanning electron microscopy (SEM) characterization verifies that the average size MoB$_2$ particles is ∼ 3.2 μm (Fig. S10). High-resolution transmission electron microscopy (HRTEM) image revels that the MoB$_2$ has high crystallinity with the lattice spacings of 0.301, 0.257 and 0.202 nm, which are indexed to (001), (100) and (101) planes of MoB$_2$, respectively (Fig. 4a). The selected area electron diffraction pattern (the inset of Fig. 4a) further confirms the presence of (001), (100) and (101) crystal planes. To determine the surface atomic valence state of MoB$_2$ particles, the X-ray photoelectron spectroscopy (XPS) spectra of Mo 3d and B 1s reveal that there are Mo^0, Mo^{3+}, Mo^{4+}, Mo^{6+}, B^0 and B^{3+} on the MoB$_2$ surface (Figs. 4b and S11) [32,46] which are in agreement with our theoretical prediction. The oxidation states of Mo and B are present
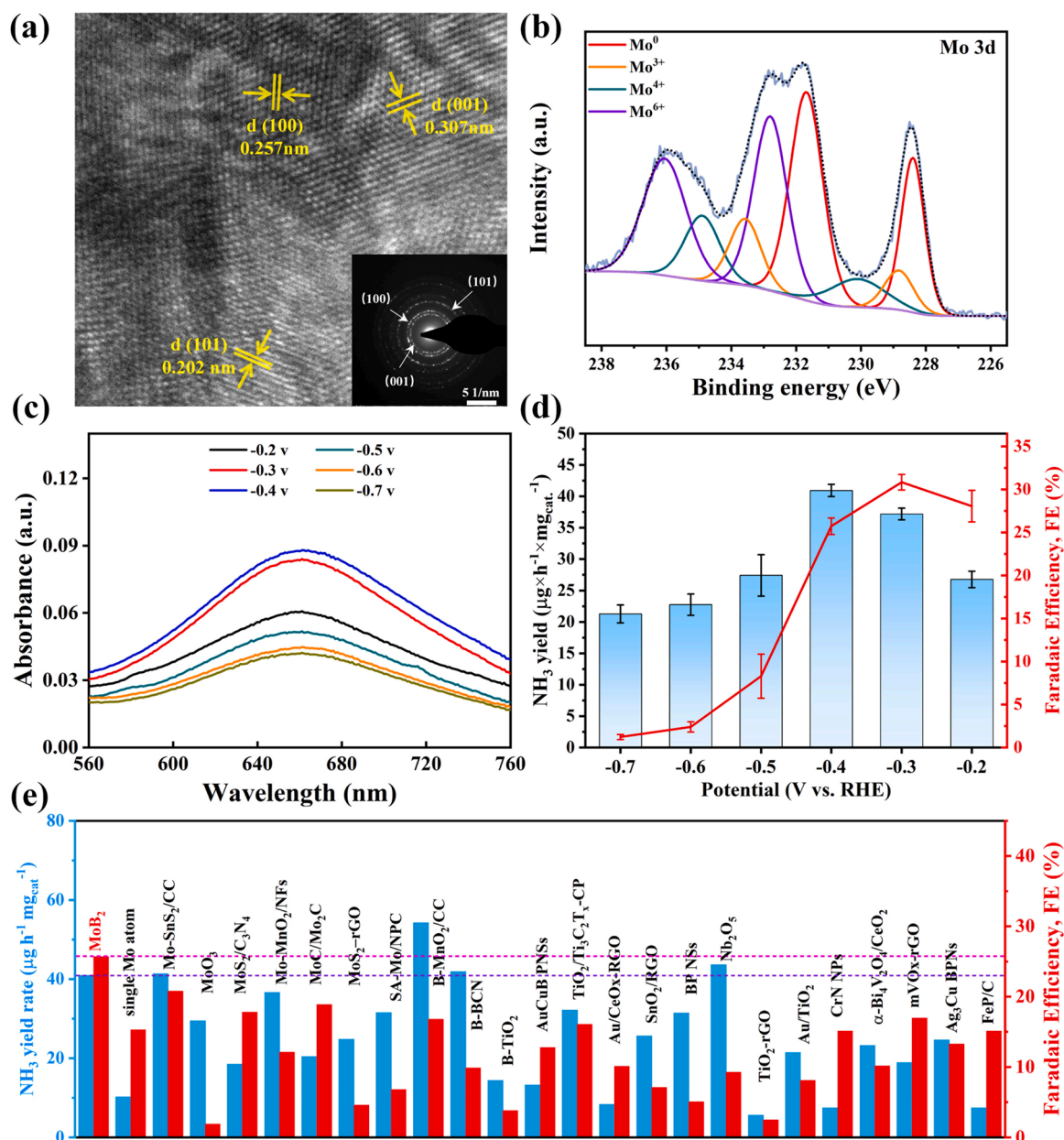
Fig. 4. (a) HRTEM image of MoB_2. Inset: the correspond SAED pattern. XPS spectra of MoB_2 in (b) Mo 3d region. (c) UV–vis absorption spectrums of the electrolytes over MoB_2 at various potentials after electrolytic reaction for 2 h. (d) NH_3 yield rate and FEs of MoB_2 under various potentials. (e) Comparison of NH_3 yield rate and FEs among MoB_2 and other reported NRR electrocatalysts.

since a part of Mo and B were oxidized by air [47]. Besides, the NRR performance of the MoB_2 catalyst was investigated in N_2-saturated 0.1 M Na_2SO_4 solution at the ambient temperature and pressure using a H-type two-compartment electrochemical cell. The MoB_2 particles were utilized as the working electrode to obtain the Linear scan voltammogram (LSV) curve (Fig. S12) and stable current density at different potentials by the chronoamperometric measurements (Fig. S13). The MoB_2 catalyst delivers a higher current density in N_2 saturated solution than in Ar-saturated solution, demonstrating the occurrence of electrochemical NRR. Based on the UV–vis absorption spectra of the electrolyte at various potentials (Fig. 4c), the established calibration curve was plotted in Fig. S14 [48]. Consequently, the corresponding NH_3 yield rate and FE at various potentials were calculated, in which the highest NH_3 yield rate of 40.94 ± 0.97 µg h^{-1} mg^{-1} and the greatest FE of $30.84 \pm 0.91\%$ are obtained at -0.4 V and -0.3 V vs. RHE (Fig. 4d). The reason for the decrease of the NH_3 yield rates and FEs of MoB_2 when the applied

potential exceeded -0.3 V vs. RHE is the appearance of a competitive adsorption of N_2 and H_2 on catalytic electrode surface, resulting in that the side-reaction (HER) becomes the primary process in this catalytic system rather than NRR [45,49].

To investigate the effect of pH changes on catalytic performance, we have evaluated the NH_3 yield rates and FEs of MoB_2 in electrolyte with various pH (0.05 M H_2SO_4 and 0.1 M KOH) at the same potential (-0.3 V vs. RHE). The established calibration curves containing different NH_3 concentrations in various electrolytes were plotted (Figs. S15 and S16). In light of the both figures, Fig. S17 is obtained. As shown in Fig. S17, both NH_3 yield rate and FE of MoB_2 in neutral electrolyte (0.1 M Na_2SO_4) are much higher than that in acid and alkaline solutions. This is mainly caused by the different concentrations of protons around the active site in solution. The high concentration of protons in acid solution increases the competitive H adsorption, whereas the low concentration of protons in alkaline solution limits the proton

transfer to NRR active sites, resulting in poor NRR performance in both solutions.

Remarkably, the MoB_2 catalyst exhibits superior catalytic activity for NRR as expected. In the meanwhile, negligible by-product N_2H_4 was detectable by the Watt and Chrisp method (Fig. S18), suggesting that MoB_2 possesses high selectivity for the electrocatalytic reduction reaction of N_2 to NH_3. Stability is also an important factor to estimate the electrocatalytic performance of the catalyst. After 12 h of continuous electrolysis, the MoB_2 catalyst displays a stable current density (Fig. S19) and maintains $\sim$ 95% retention of its initial NH_3 yield (Fig. S20), exhibiting its excellent long-term stability. Moreover, NH_3 is hardly detected when the chronoamperometric experiments are carried out at -0.4 V vs. RHE using Ar as feeding gas or at the open-circuit potential using N_2 as feeding gas (Fig. S21), denoting that the detected NH_3 is generated via NRR rather than from the contamination sources, such as laboratories, equipments, and membranes [50]. To further determine the superior NRR performance of the MoB_2 catalyst, we compared the NH_3 yield rate and FE of MoB_2 catalyst with that of representative NRR catalysts reported previously. As shown in Fig. 4e, both the NH_3 yield rate and the FE of MoB_2 are higher than that of recent literature data. Based on the above theoretical and experimental results, the MoB_2 is confirmed to be a high performance electrocatalyst for NRR, presenting promising potential for the NH_3 synthesis.

4. Conclusions

In summary, using density functional theory (DFT) calculations, we systematically investigated the potential of MoB_2 as a highly efficient and selective electrocatalyst for NRR. The synergistic effects between B and Mo atoms contribute to the introduction of electron-deficient Mo ($Mo^{\delta+}$) atom on the Mo-(001) surface of MoB_2, $Mo^{\delta+}$ as the electron-deficient active site exhibits high N_2 affinity and effective N_2 activation capacity. These improve the local concentration of N_2 around $Mo^{\delta+}$, enhance the possibility of molecular collisions, and reduce the reaction free energy of NRR process. Thus, Mo-(001) surface exhibits excellent NRR performance with low limiting potential of -0.34 V vs. RHE and the outstanding NRR selectivity that HER can be evidently retarded when negative potential is applied under actual work conditions. The above theoretical prediction is experimentally verified by using the commercial MoB_2 particles. The MoB_2 exhibits excellent NRR performance with the NH_3 yield rate of 40.94 ± 0.97 μg h^{-1} mg^{-1} at -0.4 V vs. RHE and FE of $30.84 \pm 0.91\%$ at -0.3 V vs. RHE, indicating that MoB_2 could simultaneously realize high activity and excellent selectivity for NRR.

CRediT authorship contribution statement

Hong Yu Zhou: Conceptualization, Investigation, Formal analysis, Writing – original draft. **Yan Bin Qu:** Methodology, Validation, Investigation, Writing – original draft. **Jian Chen Li:** Project administration, Writing – review & editing. **Zhi Li Wang:** Methodology, Funding acquisition. **Chun Cheng Yang:** Resources, Visualization. **Qing Jiang:** Conceptualization, Writing – review & editing, Supervision, Funding acquisition.

Declaration of Competing Interest

The authors declare that they have no known competing financial interests or personal relationships that could have appeared to influence the work reported in this paper.

Acknowledgments

Appendix A. Supporting information

Supplementary data associated with this article can be found in the online version at doi:10.1016/j.apcatb.2021.121023.

References

[1] L. Huo, X. Han, L. Zhang, B. Liu, R. Gao, B. Cao, W.W. Wang, C.J. Jia, K. Liu, J. Liu, J. Zhang, Spatial confinement and electron transfer moderating Mo—N bond strength for superior ammonia decomposition catalysis, Appl. Catal. B 294 (2021), 120254, https://doi.org/10.1016/j.apcatb.2021.120254.

[2] H. Shen, C. Choi, J. Masa, X. Li, J. Qiu, Y. Jung, Z. Sun, Electrochemical ammonia synthesis: mechanistic understanding and catalyst design, Chem 7 (2021) 1708–1754, https://doi.org/10.1016/j.chempr.2021.01.009.

[3] G. Qing, R. Ghazfar, S.T. Jackowski, F. Habibzadeh, M.M. Ashtiani, C.P. Chen, M. R. Smith III, T.W. Hamann, Recent advances and challenges of electrocatalytic N2 reduction to ammonia, Chem. Rev. 120 (2020) 5437–5516, https://doi.org/10.1021/acs.chemrev.9b00659.

[4] J.G. Chen, R.M. Crooks, L.C. Seefeldt, K.L. Bren, R.M. Bullock, M.Y. Darensbourg, P.L. Holland, B. Hoffman, M.J. Janik, A.K. Jones, M.G. Kanatzidis, P. King, K. M. Lancaster, S.V. Lymar, P. Pfromm, W.F. Schneider, R.R. Schrock, Beyond fossil fuel-driven nitrogen transformations, Science 360 (2018) 873, https://doi.org/10.1126/science.aar6611.

[5] B.H.R. Suryanto, H.L. Du, D. Wang, J. Chen, A.N. Simonov, D.R. MacFarlane, Challenges and prospects in the catalysis of electroreduction of nitrogen to ammonia, Nat. Catal. 2 (2019) 290–296, https://doi.org/10.1038/s41929-019-0252-4.

[6] Z.W. Seh, J. Kibsgaard, C.F. Dickens, I. Chorkendorff, J.K. Nørskov, T.F. Jaramillo, Combining theory and experiment in electrocatalysis: insights into materials design, Science 355 (2017) 146, https://doi.org/10.1126/science.aad4998.

[7] R. Guan, D. Wang, Y. Zhang, C. Liu, W. Xu, J. Wang, Z. Zhao, M. Feng, Q. Shang, Z. Sun, Enhanced photocatalytic N2 fixation via defective and fluoride modified TiO2 surface, Appl. Catal. B 282 (2021), 119580, https://doi.org/10.1016/j.apcatb.2020.119580.

[8] T. Dai, X. Lang, Z. Wang, Z. Wen, Q. Jiang, Rational design of an Fe cluster catalyst for robust nitrogen activation, J. Mater. Chem. A 9 (2021) 21219–21227, https://doi.org/10.1039/d1ta04638a.

[9] C. Tang, S.Z. Qiao, How to explore ambient electrocatalytic nitrogen reduction reliably and insightfully, Chem. Soc. Rev. 48 (2019) 3166–3180, https://doi.org/10.1039/c9cs00280d.

[10] S. Liu, T. Qian, M. Wang, H. Ji, X. Shen, C. Wang, C. Yan, Proton-filtering covalent organic frameworks with superior nitrogen penetration flux promote ambient ammonia synthesis, Nat. Catal. 4 (2021) 322–331, https://doi.org/10.1038/s41929-021-00599-w.

[11] X. Yu, P. Han, Z. Wei, L. Huang, Z. Gu, S. Peng, J. Ma, G. Zheng, Boron-doped graphene for electrocatalytic N2 reduction, Joule 2 (2018) 1610–1622, https://doi.org/10.1016/j.joule.2018.06.007.

[12] J. Lan, M. Luo, J. Han, M. Peng, H. Duan, Y. Tan, Nanoporous B13 C2 towards highly efficient electrochemical nitrogen fixation, Small 17 (2021) 2102814, https://doi.org/10.1002/smll.202102814.

[13] J. Long, X. Fu, J. Xiao, The rational design of single-atom catalysts for electrochemical ammonia synthesis via a descriptor-based approach, J. Mater. Chem. A 8 (2020) 17078–17088, https://doi.org/10.1039/d0ta05943a.

[14] Y. Chen, G. Yu, W. Chen, Y. Liu, G.D. Li, P. Zhu, Q. Tao, Q. Li, J. Liu, X. Shen, H. Li, X. Huang, D. Wang, T. Asefa, X. Zou, Highly active, nonprecious electrocatalyst comprising borophene subunits for the hydrogen evolution reaction, J. Am. Chem. Soc. 139 (2017) 12370–12373, https://doi.org/10.1021/jacs.7b06337.

[15] P.R. Jothi, K. Yubuta, B.P.T. Fokwa, A simple, general synthetic route toward nanoscale transition metal borides, Adv. Mater. 30 (2018) 1704181, https://doi.org/10.1002/adma.201704181.

[16] H. Park, A. Encinas, J.P. Scheifers, Y. Zhang, B.P.T. Fokwa, Boron-dependency of molybdenum boride electrocatalysts for the hydrogen evolution reaction, Angew. Chem. Int. Ed. 56 (2017) 5575–5578, https://doi.org/10.1002/anie.201611756.

[17] M.D. Segall, Philip J.D. Lindan, M.J. Probert, C.J. Pickard, P.J. Hasnip, S.J. Clark, M.C. Payne, Condensed matter first-principles simulation: ideas, illustrations and the CASTEP code, J. Phys.: Condens. Matter 14 (2002) 2717–2744, https://doi.org/10.1088/0953-8984/14/11/301.

[18] D. Vanderbilt, Soft self-consistent pseudopotentials in a generalized eigenvalue formalism, Phys. Rev. B 41 (1990) 7892–7895, https://doi.org/10.1103/PhysRevB.41.7892.

[19] J.P. Perdew, K. Burke, M. Ernzerhof, Generalized gradient approximation made simple, Phys. Rev. Lett. 77 (1996) 3865–3868, https://doi.org/10.1103/PhysRevLett.77.3865.

[20] S. Grimme, Semiempirical gga-type density functional constructed with a long-range dispersion correction, J. Comput. Chem. 27 (2006) 1787–1799, https://doi.org/10.1002/jcc.20495.

[21] R. Dronskowski, P.E. Bloechl, Crystal orbital hamilton populations (cohp): energy-resolved visualization of chemical bonding in solids based on density-functional

calculations, J. Phys. Chem. 97 (2002) 8617–8624, https://doi.org/10.1021/j100135a014.

[22] V.L. Deringer, A.L. Tchougreeff, R. Dronskowski, Crystal orbital hamilton population (cohp) analysis as projected from plane-wave basis sets, J. Phys. Chem. A 115 (2011) 5461–5466, https://doi.org/10.1021/jp202489s.

[23] S. Maintz, V.L. Deringer, A.L. Tchougreeff, R. Dronskowski, Lobster: a tool to extract chemical bonding from plane-wave based DFT, J. Comput. Chem. 37 (2016) 1030–1035, https://doi.org/10.1002/jcc.24300.

[24] S. Haider, A. Roldan, N.H. de Leeuw, Catalytic dissociation of water on the (001), (011), and (111) surfaces of violarite, FeNi2S4: a DFT-D2 study, J. Phys. Chem. C 118 (2014) 1958–1967, https://doi.org/10.1021/jp409522q.

[25] J.H. Montoya, C. Tsai, A. Vojvodic, J.K. Nørskov, The challenge of electrochemical ammonia synthesis: a new perspective on the role of nitrogen scaling relations, ChemSusChem 8 (2015) 2180–2186, https://doi.org/10.1002/cssc.201500322.

[26] J.K. Nørskov, J. Rossmeisl, A. Logadottir, L. Lindqvist, J.R. Kitchin, T. Bligaard, H. Jónsson, Origin of the overpotential for oxygen reduction at a fuel-cell cathode, J. Phys. Chem. B 108 (2004) 17886–17892, https://doi.org/10.1021/jp047349j.

[27] E. Skulason, T. Bligaard, S. Gudmundsdottir, F. Studt, J. Rossmeisl, F. Abild-Pedersen, T. Vegge, H. Jonsson, J.K. Nørskov, A theoretical evaluation of possible transition metal electro-catalysts for N2 reduction, Phys. Chem. Chem. Phys. 14 (2012) 1235–1245, https://doi.org/10.1039/c1cp22271f.

[28] W.M. Haynes, CRC Handbook of Chemistry and Physics, CRC Press/Taylor and Francis, Boca Raton, FL, 2016, p. 876.

[29] L. Shi, Y. Yin, S. Wang, X. Xu, H. Wu, J. Zhang, S. Wang, H. Sun, Rigorous and reliable operations for electrocatalytic nitrogen reduction, Appl. Catal. B 278 (2020), 119325, https://doi.org/10.1016/j.apcatb.2020.119325.

[30] X. Li, T. Li, Y. Ma, Q. Wei, W. Qiu, H. Guo, X. Shi, P. Zhang, A.M. Asiri, L. Chen, B. Tang, X. Sun, Boosted electrocatalytic N2 reduction to NH3 by defect-rich MoS2 nanoflower, Adv. Energy Mater. 8 (2018) 1801357, https://doi.org/10.1002/aenm.201801357.

[31] G.W. Watt, J.D. Chrisp, Spectrophotometric method for determination of hydrazine, Anal. Chem. 24 (1952) 2006–2008, https://doi.org/10.1021/ac60072a044.

[32] H. Park, Y. Zhang, J.P. Scheifers, P.R. Jothi, A. Encinas, B.P.T. Fokwa, Graphene- and phosphorene-like boron layers with contrasting activities in highly active Mo2B4 for hydrogen evolution, J. Am. Chem. Soc. 139 (2017) 12915–12918, https://doi.org/10.1021/jacs.7b07247.

[33] Z.W. Chen, Z. Lu, L.X. Chen, M. Jiang, D. Chen, C.V. Singh, Machine-learning-accelerated discovery of single-atom catalysts based on bidirectional activation mechanism, Chem. Catal. 1 (2021) 183–195, https://doi.org/10.1016/j.checat.2021.03.003.

[34] X. Lv, W. Wei, B. Huang, Y. Dai, T. Frauenheim, High-throughput screening of synergistic transition metal dual-atom catalysts for efficient nitrogen fixation, Nano Lett. 21 (2021) 1871–1878, https://doi.org/10.1021/acs.nanolett.0c05080.

[35] X. Liu, Y. Jiao, Y. Zheng, S.Z. Qiao, Isolated boron sites for electroreduction of dinitrogen to ammonia, ACS Catal. 10 (2020) 1847–1854, https://doi.org/10.1021/acscatal.9b04103.

[36] Z.W. Chen, L. Chen, M. Jiang, D. Chen, Z. Wang, X. Yao, C.V. Singh, Q. Jiang, Triple atom catalyst with ultrahigh loading potential for nitrogen electrochemical reduction, J. Mater. Chem. A (2020), https://doi.org/10.1039/d0ta04919k.

[37] Y. Guo, Z. Yao, S. Zhan, B.J.J. Timmer, C.W. Tai, X. Li, Z. Xie, Q. Meng, L. Fan, F. Zhang, M.S.G. Ahlquist, M. Cuartero, G.A. Crespo, L. Sun, Molybdenum and boron synergistically boosting efficient electrochemical nitrogen fixation, Nano Energy 78 (2020), 105391, https://doi.org/10.1016/j.nanoen.2020.105391.

[38] S. Zheng, S. Li, Z. Mei, Z. Hu, M. Chu, J. Liu, X. Chen, F. Pan, Electrochemical nitrogen reduction reaction performance of single-boron catalysts tuned by mxene substrates, J. Phys. Chem. Lett. 10 (2019) 6984–6989, https://doi.org/10.1021/acs.jpclett.9b02741.

[39] Y. Gu, B. Xi, W. Tian, H. Zhang, Q. Fu, S. Xiong, Boosting selective nitrogen reduction via geometric coordination engineering on single-tungsten-atom catalysts, Adv. Mater. (2021) 2100429, https://doi.org/10.1002/adma.202100429.

[40] H. Vrubel, X. Hu, Molybdenum boride and carbide catalyze hydrogen evolution in both acidic and basic solutions, Angew. Chem. Int. Ed. 51 (2012) 12703–12706, https://doi.org/10.1002/anie.201207111.

[41] A.R. Singh, B.A. Rohr, J.A. Schwalbe, M. Cargnello, K. Chan, T.F. Jaramillo, I. Chorkendorff, J.K. Nørskov, Electrochemical ammonia synthesis—the selectivity challenge, ACS Catal. 7 (2016) 706–709, https://doi.org/10.1021/acscatal.6b03035.

[42] X. Yao, Z.W. Chen, Y. Wang, X. Lang, W. Gao, Y. Zhu, Q. Jiang, Activated basal plane of WS2 by intrinsic defects as a catalyst for electrocatalytic nitrogen reduction reaction, J. Mater. Chem. A 7 (2019) 25961–25968, https://doi.org/10.1039/c9ta10050d.

[43] X. Liu, Y. Jiao, Y. Zheng, M. Jaroniec, S.Z. Qiao, Building up a picture of the electrocatalytic nitrogen reduction activity of transition metal single-atom catalysts, J. Am. Chem. Soc. 141 (2019) 9664–9672, https://doi.org/10.1021/jacs.9b03811.

[44] L. Li, J.M.P. Martirez, E.A. Carter, Prediction of highly selective electrocatalytic nitrogen reduction at low overpotential on a mo-doped g-gan monolayer, ACS Catal. 10 (2020) 12841–12857, https://doi.org/10.1021/acscatal.0c03140.

[45] C. Choi, G.H. Gu, J. Noh, H.S. Park, Y. Jung, Understanding potential-dependent competition between electrocatalytic dinitrogen and proton reduction reactions, Nat. Commun. 12 (2021) 4353, https://doi.org/10.1038/s41467-021-24539-1.

[46] J. Zhang, X. Tian, M. Liu, H. Guo, J. Zhou, Q. Fang, Z. Liu, Q. Wu, J. Lou, Cobalt-modulated molybdenum–dinitrogen interaction in MoS2 for catalyzing ammonia synthesis, J. Am. Chem. Soc. 141 (2019) 19269–19275, https://doi.org/10.1021/jacs.9b02501.

[47] L. Han, X. Liu, J. Chen, R. Lin, H. Liu, F. Lü, S. Bak, Z. Liang, S. Zhao, E. Stavitski, J. Luo, R.R. Adzic, H.L. Xin, Atomically dispersed molybdenum catalysts for efficient ambient nitrogen fixation, Angew. Chem. Int. Ed. 58 (2019) 2321–2325, https://doi.org/10.1002/anie.201811728.

[48] L. Zhang, X. Ji, X. Ren, Y. Ma, X. Shi, Z. Tian, A.M. Asiri, L. Chen, B. Tang, X. Sun, Electrochemical ammonia synthesis via nitrogen reduction reaction on a MoS2 catalyst: theoretical and experimental studies, Adv. Mater. 30 (2018) 1800191, https://doi.org/10.1002/adma.201800191.

[49] N. Cao, Z. Chen, K. Zang, J. Xu, J. Zhong, J. Luo, X. Xu, G. Zheng, Doping strain induced bi-Ti(3+) pairs for efficient N2 activation and electrocatalytic fixation, Nat. Commun. 10 (2019) 2877, https://doi.org/10.1038/s41467-019-10888-5.

[50] D. Zhang, H. Zhao, X. Wu, Y. Deng, Z. Wang, Y. Han, H. Li, Y. Shi, X. Chen, S. Li, J. Lai, B. Huang, L. Wang, Multi-site electrocatalysts boost pH-universal nitrogen reduction by high-entropy alloys, Adv. Funct. Mater. 31 (2021) 2006939, https://doi.org/10.1002/adfm.202006939.